

AJ Thornton, G Fishpool, A Kirk and the MAST Team

The Effect of L mode Filaments on Divertor Heat Flux Profiles as Measured by Infrared Thermography on MAST

Enquiries about copyright and reproduction should in the first instance be addressed to the Culham Publications Officer, Culham Centre for Fusion Energy (CCFE), K1/083, Culham Science Centre, Abingdon, Oxfordshire, OX14 3DB, UK. The United Kingdom Atomic Energy Authority is the copyright holder.

The Effect of L mode Filaments on Divertor Heat Flux Profiles as Measured by Infrared Thermography on MAST

AJ Thornton¹, G Fishpool¹, A Kirk¹ and the MAST Team

¹*CCFE, Culham Science Centre, Abingdon, Oxon, OX14 3DB, UK*

The effect of L mode filaments on divertor heat flux profiles as measured by infrared thermography on MAST

AJ Thornton¹, G Fishpool¹, A Kirk¹ and the MAST Team

¹CCFE, Culham Science Centre, Abingdon, Oxon, OX14 3DB, UK

E-mail: andrew.thornton@ccfe.ac.uk

Abstract. Filamentary transport across the scrape off layer is a key issue for the design and operation of future devices, such as ITER, DEMO and MAST-U, as it sets the power loadings to the divertor and first wall of the machine. Analysis has been performed on L mode filaments in MAST in order to gain an understanding of the spatial structure and attempt to reconcile the different scales of the filament width and the power fall off length (λ_q). The L mode filament heat flux arriving at the divertor has been measured using high spatial resolution (1.5 mm) infrared (IR) thermography. The filaments form discrete spiral patterns at the divertor which can be seen as bands of increased heat flux in the IR measurements. Analysis of the width and spacing of these bands at the divertor has allowed the toroidal mode number of the filaments to be determined ($7 \leq n \leq 22$). The size of the filaments at the midplane has been determined using the target filament radial width and the magnetic field geometry. The filament width perpendicular to the magnetic field at the midplane has been found to be between 3 and 5 cm. Direct calculation of the filament width from midplane visible imaging gives a range of 4-6 cm which agrees well with the IR data.

PACS numbers: 52.55.Fa, 52.55.Rk, 52.70.-m

Submitted to: *Plasma Phys. Control. Fusion*

19 March 2015

1. Introduction

An understanding of plasma transport across the magnetic field in tokamaks is a vital for the design of future devices as it determines the heat and particle fluxes arriving at the first wall. The transport of plasma across the magnetic field had been thought to be driven by steady state diffusive processes, however, upon detailed inspection the boundary of fusion devices is significantly more turbulent [1] and exhibits intermittent events which expel heat and particles from the plasma. These intermittent events take the form of filaments which have been observed on several devices via visible imaging [2, 3]. The visible imaging shows that the filaments are emitted from the plasma edge and ejected into the scrape off layer (SOL) [4]. The intermittent events have also been extensively studied using reciprocating probe measurements on JET [5], DIII-D [6], ASDEX Upgrade [7, 8], Tore Supra [9] and also MAST [10]. These studies have confirmed the existence of intermittent events that originate from the plasma edge and extend into the scrape off layer (SOL) and are responsible for affecting the decay of the plasma density and temperature in the SOL. In addition to these experimental studies, numerical modelling has validated the results observed and provided support for the intermittent events being caused by filaments of plasma travelling out into the SOL [11, 12]. An understanding of the effect these filaments have on divertor target profiles and cross field transport is an important area of research, enabling increased understanding of the area over which the power is deposited onto the divertor and first wall. The quantity of power carried by filaments is a key issue when designing a new machine with close fitting vessel structure, such as MAST Upgrade [13], where significant power loads could be deposited onto first wall regions if the filament transport is not fully taken into account. This is especially the case in ITER, with the use of beryllium walls which have a lower level of power handling compared to tungsten, the power deposited outside the divertor region could affect the lifetime or performance of the divertor in these future devices.

Previously on MAST, experimental measurements have been made using visible imaging to analyse the distribution, size and motion of the filaments as they leave the midplane plasma edge [14, 15]. It is widely observed that edge localised mode (ELMs) are filamentary in nature [16], but it has been shown that filaments exist in L mode and inter-ELM H mode phases of the plasma with the filaments in each phase having different properties. The largest filaments which occur in steady state conditions (discharges without ELMs) are observed in L mode plasmas, with intensities in visible light of double those of inter-ELM filaments [14]. In contrast to the L mode filaments, the smaller and faster inter-ELM filaments are hardly measureable with the current MAST IR system. Therefore, we concentrate on the characterisation of the L mode filaments in this study. The typical sizes of the L mode filaments are 5-10 cm radially at the midplane [15], which is much larger than the observed heat flux fall off length measured by Langmuir probes [17] and infrared (IR) measurements [18]. The substantial difference between the observed filament size and the heat flux fall off length, over which

the majority of the power is exhausted, is an area of interest for the design of MAST-U. The divertor chamber entrance is designed to carry sufficient midplane flux into the divertor chamber to deposit the power onto the divertor surfaces, but have a sufficiently narrow area that a high neutral compression ratio can be obtained between the main chamber and divertor volume. The large differences in the filament size and fall off length greatly affect the choice of divertor entrance area. One aim of this analysis is to determine whether power is carried mainly by the filaments or over the fall off length.

The paper is structured as follows; section 2 will describe the experimental measurements made to identify the filaments at the divertor, these identified filaments will then be analysed using the techniques outline in section 3. Section 4 will aim to relate the target IR measurements to the filaments at the midplane, allowing a comparison of the filament properties in the IR and the previous visible imaging studies to be performed in section 5. Finally the paper will conclude with section 6.

2. Experimental identification of filaments at the target

2.1. IR thermography on MAST for imaging filaments

The IR system on MAST is designed to routinely measure the heat flux deposited onto the divertor surfaces by the plasma [18]. The results presented in this paper utilise measurements made in the medium wavelength IR range (4.5-5.0 μm). The spatial resolution of the standard IR system has been improved in these studies to better resolve the L mode filaments which arrive at the divertor, and have smaller heat fluxes and radial extents than the ELM filaments previously studied [16]. The imaged region of the divertor covers 0.4 m in radius at a spatial resolution of 1.6 mm and monitors the heat load to two adjacent divertor tiles of the lower outer divertor, as shown by the dashed box in figure 1. Previous measurements [14] have shown that the filaments have lifetimes of the order 40-60 μs , as a result if the IR emission from the divertor is averaged over a period longer than this, then the filaments spatial structure will be averaged out. In order to prevent blurring of the filaments from the integration time and provide sufficient signal to detect the filament heat flux, the integration time for the data used in this study is required to be less than 30 μs . The IR camera can be operated at frame rates of up to 5 kHz. The tracking of the filaments from frame to frame in the IR data is prevented by the maximum frame rate of the camera which is capable of a frame every 200 μs , or around four times the duration of an individual filament event. The camera integration time determines if the filaments can be seen on the divertor.

2.2. Observations of filaments in MAST IR data

The L mode filaments in a given shot carry a certain fraction of power down to the divertor, therefore, the larger the filament, the higher the level of power. In order to understand the signature of a filament in the divertor in the IR, discharges with a large amount of input power have been selected. These discharges are the most likely to have

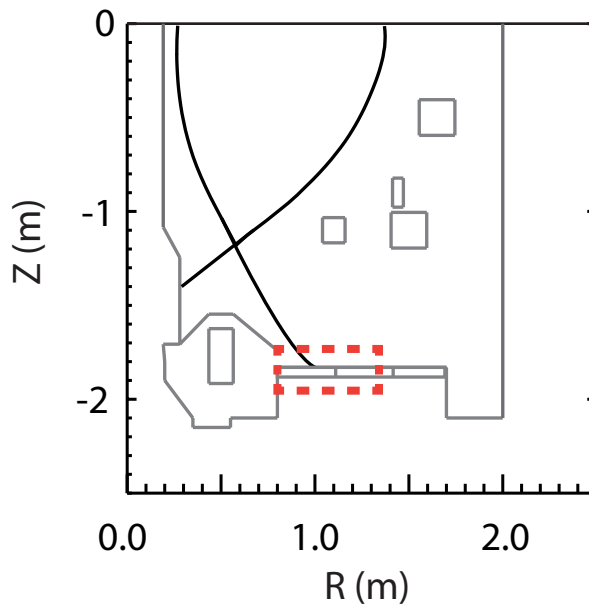


Figure 1. Lower divertor view in MAST, showing the outline of the plasma in black and the vessel walls in grey. The dashed red region corresponds to the view of the IR camera used in the analysis presented in this paper.

a sufficient level of power in the filaments to make them clearly visible at the divertor. A systematic survey for discharges with high target power loads at the lower outer divertor has identified a lower single null (LSN) plasma which exhibits clear filaments in the IR data. An example of the heat flux recorded on the IR camera at the lower outer divertor of an L mode LSN plasma, with a plasma current of 800 kA and input neutral beam power of 3.7 MW is shown in figure 2. Figure 2 shows the evolution of the divertor power load as a function of time along the abscissa and radius along the ordinate. The strike point can be seen to sweep outwards as the discharge progresses due to the stray field from the solenoid. The filamentary nature of the power arriving at the target can be seen by the striations in magnitude of the heat flux in the radial and time directions on this figure.

A single time point can be selected from the data shown in figure 2 and the raw image recorded on the IR camera plotted to show the structure of the filaments at the divertor. This IR image is shown in figure 3 a) and shows filaments present in the IR data. In the case shown here, the exposure time of the camera is 28 μ s, with a frame rate of 900 Hz. The image has been background subtracted to remove the counts associated with the ambient temperature of the divertor tiles. The white arrow denotes the location of a tile gap in the divertor which is located at $R = 1.05$ m. Figure 3 a) shows clear filamentary structures on the scrape off layer side of the divertor (left hand side of the figure). The filaments become more easily distinguished from the main strike point (right hand side of the figure) as the radius across the divertor increases. The profile shown in figure 3 b) is a profile of the IR counts extracted from panel a) along the dashed blue line, the orientation of the camera is such that the left hand side of the

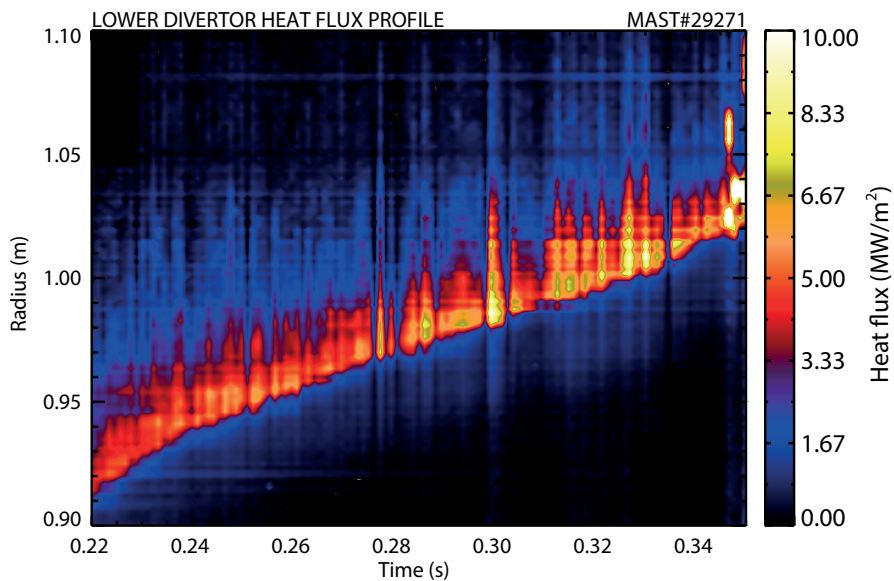


Figure 2. Heat flux to the lower outer divertor recorded using infrared thermography. The x axis is the time through the discharge and the y axis is the radius. The motion of the strike point is due to the stray field from the solenoid leading to strike point sweeping.

profile is the SOL region. The green dot dashed lines map the filaments seen in the raw image to the peaks generated by the filaments in the profile. It can be seen that there are clear peaks in the profile for each of the filaments observed in the raw image above the threshold level. The threshold level is set by the amplitude of the profile exceeding the standard deviation of the background (dark pixel) level.

The temporal history of the surface temperature recorded by the IR camera is converted to the divertor heat flux using the THEODOR code [19]. The determination of the heat flux involves the differential of the temperature history in time and space, which can introduce noise to the heat flux profiles above that generated by the camera itself. Figure 4 a) shows the profile extracted from the raw camera imaged mapped into machine coordinates and normalised to the location of the last closed flux surface (LCFS). The filaments can be seen clearly in the raw profile at this stage. Figure 4 b) shows the profile converted into heat flux at the divertor. Comparison of the raw counts profile and the heat flux profile clearly shows that any noise introduced by the derivation of the heat flux does not obscure the signature of the filaments in the profile. The filaments are seen in this profile most clearly between $0.07 < \Delta R_{LCFS} < 0.12$ m, where ΔR_{LCFS} is the distance from the peak of the heat flux which is taken as the location of the LCFS. Additional structure in the heat flux profile is seen in the near fall off length between $0.0 < \Delta R_{LCFS} < 0.07$ m, where a number of filaments are amplified in magnitude upon conversion from raw counts to heat flux.

The profiles of the heat flux to the divertor can be affected by surface effects, such as gaps and hotspots [20] on the tiles themselves. These features appear as peaks or troughs in the heat flux profiles and could be mistaken for filaments. Figure 5 shows

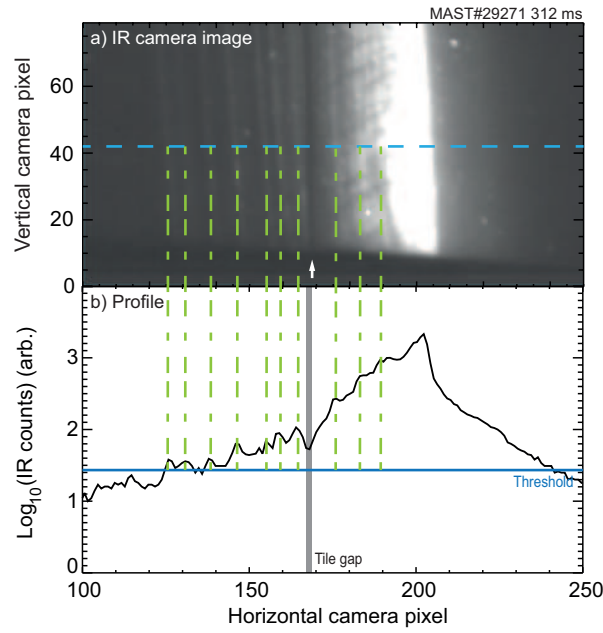


Figure 3. a) Raw IR camera counts, background subtracted and plotted on a log scale showing filaments at the divertor. The horizontal camera pixel corresponds to the radial direction across the divertor and the vertical camera pixel corresponds to the toroidal direction. b) The IR camera counts profile along the blue dashed line in panel a). The solid blue line corresponds to the signal to noise is one. The grey vertical bar is the location of the tile gap. The radius increases to the left in the figure above, due to the orientation of the camera.

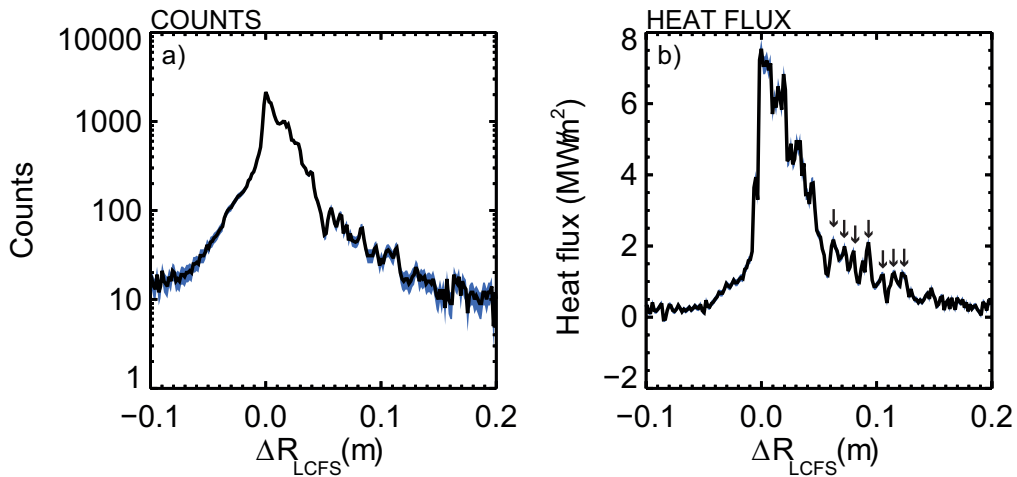


Figure 4. a) An IR profile taken from the IR camera in raw camera counts and mapped into machine coordinates. b) The heat flux to the divertor extracted from the analysed raw IR data at the same time of the raw profile in a). The radial coordinate is normalised to the position of the last closed flux surface (LCFS) in both plots. The blue shaded region in each panel represents the error on the measurement and the arrows region in panel b) represent the location of the identified filaments.

the single IR profile showing filaments (red line) and an averaged heat flux profile over a period of 5 ms around the single frame (blue line, with circles). The grey bars on the averaged data profile are the one sigma errors associated with the variance of the heat flux at a given radius. It can be seen by comparing the averaged profile with the single profile, that the filaments previously identified are not present in the average profile. Surface features such as hotspots that affect the profiles are static in time and would give a fixed peak at a given location when averaged together, as the averaged profile does not show this, it gives confidence that the peaks observed in the IR profiles are generated by the arrival at the target of filaments ejected from the midplane and not an artifact of the surface being imaged.

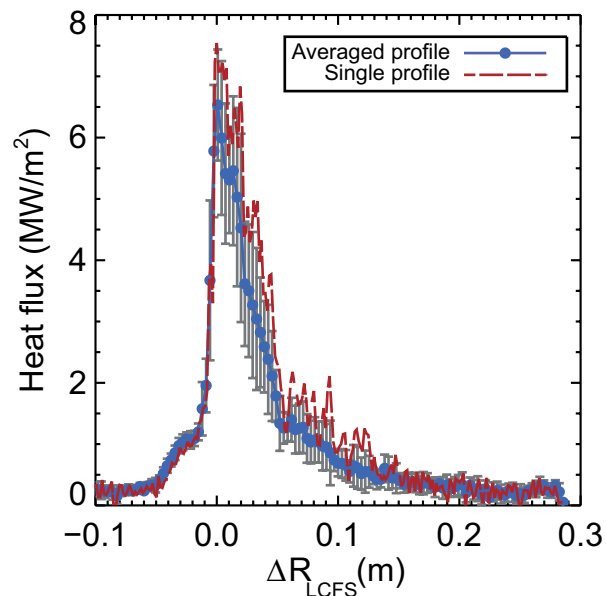


Figure 5. Temporal averaged profiles at the target for 5 time points either side of the filamentary profile in 29271. The averaged profile is shown with the solid line and blue dots and the single profile at 312ms is shown as the dashed red line. The error bars on the averaged profile correspond to the standard deviation of the profiles at a given radial location.

The analysis of the heat flux to the divertor target during a filament requires careful consideration due to the frame rate and integration time of the IR camera. The IR camera frame rate used here has a period of 1 ms between frames during which time a filament may arrive and heat the divertor which would add to the background level. The short integration time of $30 \mu\text{s}$ also means that the IR data could capture the initial phase, peak or tail of the filament heat flux. Therefore, there will be variation in the filament heat flux to the target. The integrated nature of the measurements therefore make it difficult to exactly separate the filament heat flux from the background, as this would require that the IR camera operated at timescales on par with the filament events and that the temperature of the divertor responded rapidly to changes in the heat flux. The addition of some filament events to the background prevents the relative

magnitude of the filament power and the non-filamentary power from being compared. However, the absolute magnitude of the filament heat flux can be found and on average the peak filament heat flux can be determined from the measurements. The location of the filaments in the profiles can be identified using a time average of the IR profiles and determining the variation from the average. The average heat flux profile, \bar{q} , as defined by equation 1 is shown in figure 6. The analysis of the L mode filaments requires IR data from period in the discharge after the formation of the divertor and without any transient events. In the discharge analysed here, a period of approximately 100 ms is suitable for analysis based on these criteria. The average is performed over a 50 ms period of the data shown in figure 2 where a profile is recorded at a frequency of 1 kHz. The average heat flux profile is fitted using an Eich function [21] to determine the fall off length at the midplane, $\lambda_q = 6.3$ mm. The average profile can be subtracted from the individual profiles over the selected time window and the root mean square fluctuation ($\delta\bar{q}$) determined (equation 2) which is plotted against the distance from the LCFS in figure 6 (red circles). The fluctuation can be seen to be concentrated in the region from the LCFS into the SOL, with a constant level of fluctuation seen in across this region.

$$\bar{q} = \bar{q}(r) = \frac{1}{m} \sum_{i=t_{st}}^{t_{end}} q(r, t_i) \quad (1)$$

$$\delta\bar{q} = \delta\bar{q}(r) = \left(\frac{1}{m} \sum_{i=t_{st}}^{t_{end}} [q(r, t_i) - \bar{q}]^2 \right)^{\frac{1}{2}} \quad (2)$$

3. Filament analysis

Analysis of the filaments requires them to be located and extracted from the heat flux profiles. The extraction of the filaments from the IR profiles allows two features of the filaments to be found: the radial separation between filaments at the divertor and the filament full width half maximum (FWHM) to determine the radial filament size at the divertor.

Filaments arriving at the divertor can clearly be seen in the IR data, and the raw camera images are inspected during the 100 ms transient free period to select frames which contain filaments. The heat flux profiles corresponding to these IR frames are extracted and the location of the peak filament heat flux identified. The minima corresponding to the filament peaks can then be determined from the profile. The filament heat flux is extracted from the heat flux profile subtracting the background heat flux which is found via fitting of the heat flux profile with the identified filament points removed. The process of extracting the filaments can be seen in figure 7 where the black dot-dashed trace is the original heat flux profile. The minima of the peaks are then used to remove the filaments from the profiles, leaving the background profile only (red circles), which can be fitted with an Eich function [21] to provide a background heat flux (blue dashed curve) which is then subtracted from the original heat flux profile

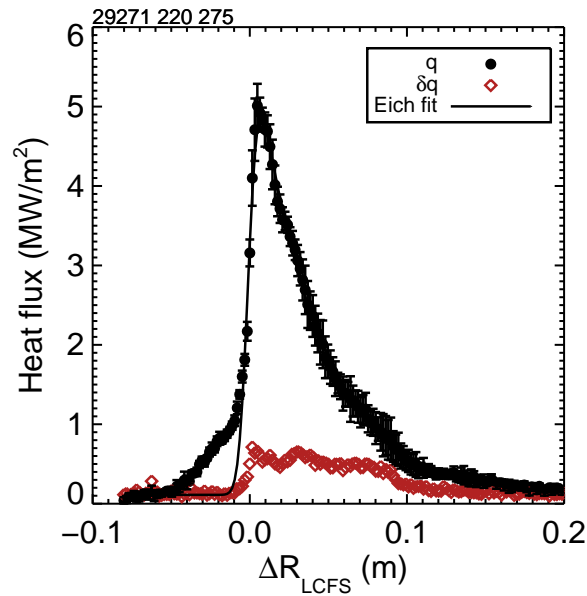


Figure 6. The average profiles shown in black circles and fitted using an Eich fit, alongside the summed root mean square (RMS) fluctuations of the profiles composing the average. b) The ratio of the RMS fluctuation and the average profile as a function of distance from the LCFS. The IR profile is seen to broaden out into the PFR, this is observed on MAST IR data and is possibly generated as an artefact of the strike point sweeping.

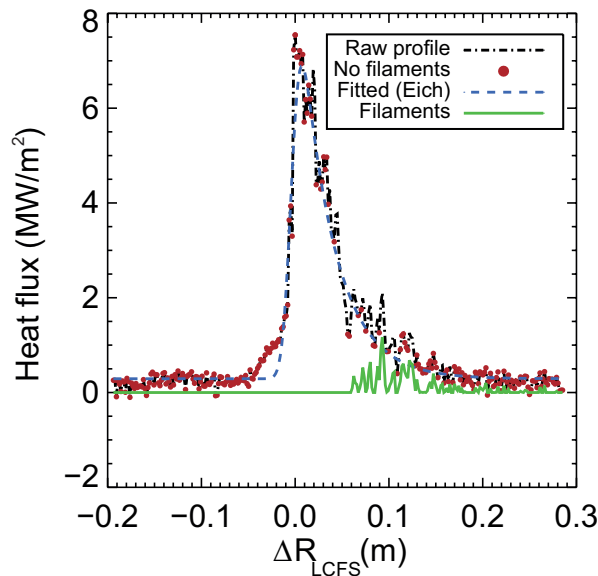


Figure 7. Analysis of the filamentary part of the heat flux profile by extracting the filament component. The black curve is the heat flux profile at the divertor, the red points are the points in the heat flux profile excluding the filaments. The filaments (green curve) are extracted by subtracting the fitted Eich curve (blue) from the IR profile (black).

to leave the filament contribution (solid green line). The variations in the heat flux at $\Delta R_{LCFS} \leq 0.05$ have been removed from the analysis of the filaments. The filaments have been removed in this region as the toroidal rotation and magnetic shear cause the filaments where $\delta R_{LCFS} \leq 0.05$ m to blend together, as will be described in section 5.4. As a result of the filaments merging into one, the width and heat flux of an individual filament structure cannot be identified in this region.

The filament width is determined by extracting the points between the two minima either side of a filament maximum and fitting a Gaussian profile. The width of the filament at the target, δr_{tgt} , is defined as the full width half maximum of the Gaussian; $\delta r_{tgt} = 2\sigma_{fit}\sqrt{2\ln 2}$, where σ_{fit} is the fitted Gaussian width. Analysis of the data in such a manner, and rejection of filaments where there are insufficient data points to extract a width, gives 70 individual filaments from the 17 profiles selected in the time window. The filament width extracted from the IR data in the L mode shot analysed in this paper is shown in figure 8 and the modal width lying in the range 4-6 mm.

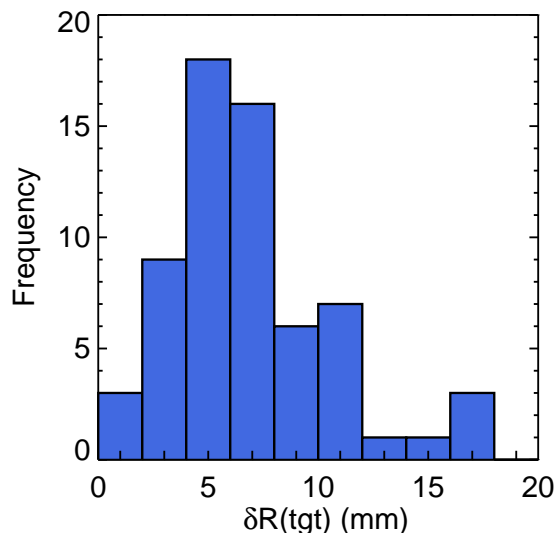


Figure 8. Histogram of the radial filament size as measured at the target, δR_{tgt} , for a number of IR profiles exhibiting filaments.

The filament separation extracted from the same profiles where the filament width has been found is shown in figure 9. The modal filament spacing lies between 15-18mm, which is around three times the filament width at the divertor in these profiles.

The filaments carry heat flux to the divertor, in the region where the profiles have been analysed for the filament size and separation, the filament heat flux can also be determined given the limitations discussed in section 2.2. The outer fall off of the heat flux profile ($\Delta R_{LCFS} > 0.05$ m) is used to analyse the heat flux, as individual filaments can be resolved in this region without the blurring brought about by the magnetic geometry and toroidal rotation. The typical heat flux of the filaments in this region is between 0.6 and 0.8 MW/m², and they carry the average of 0.14(± 0.1) MW of power

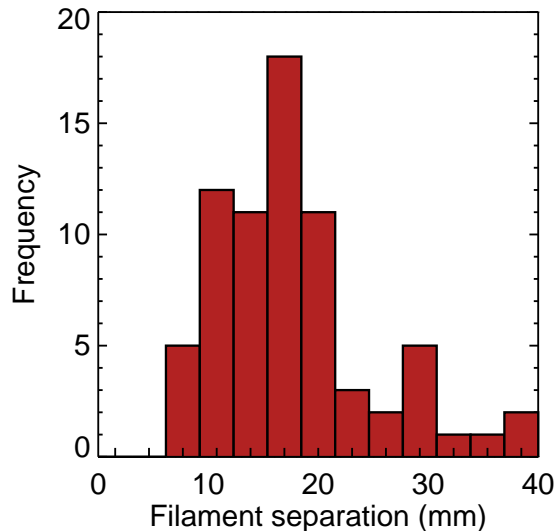


Figure 9. Histogram of the separation between filament peaks in the profiles where the filaments have been identified.

to the target in a given profile.

4. Relating the divertor filament size to the midplane

The measurements from the IR data are performed at the target, whereas previous visible imaging data, where the filament size has been determined, were made at the midplane. The conversion of the IR data at the target to the midplane allows the visible and IR measurements to be compared directly. The filamentary structure at the divertor can be mapped to the midplane using the equilibrium magnetic field to allow the midplane filament size to be derived from the target IR measurements. This technique has been used previously to investigate the IR footprint from ELMs at the divertor [16].

4.1. Field parameterisation

Figure 10 shows the result of mapping between a set of radial points on the divertor, at fixed toroidal angle, to the midplane. The mapping is generated by following field lines from a set of points radially across the target to the midplane and determining the toroidal angle that has been travelled between the start and end points. The equilibrium magnetic field is determined using EFIT reconstruction of the plasma [22]. The radial points are spread over a 15 mm region of the divertor and are located 5 cm away from the LCFS at the target. The dashed line shows the location of the LCFS at the target. The field lines can clearly be seen to map to the midplane and extend over a toroidal section of the midplane circumference (dot dashed line). There is some variation in the midplane radius of the mapped points, however this is significantly smaller than the

toroidal displacement that is seen through the field line tracing. Taking into account the effect of mapping from the divertor to the midplane, a radial displacement at the target gives rise to a toroidal displacement at the midplane. The connection between the midplane toroidal angle and the target radius has been made during ELM studies to determine the toroidal mode number [23, 24] which will be described in section 5.

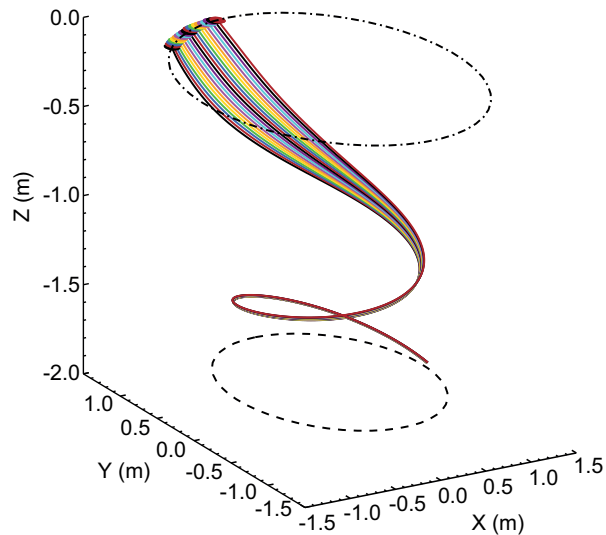


Figure 10. Mapping of a radial set of points at the divertor to the midplane using field line tracing. The radial set of points at the divertor covers a region of 15 mm at a fixed toroidal angle located 5 cm from the LCFS. The mapped points at the midplane cover a range of toroidal angles at similar radii.

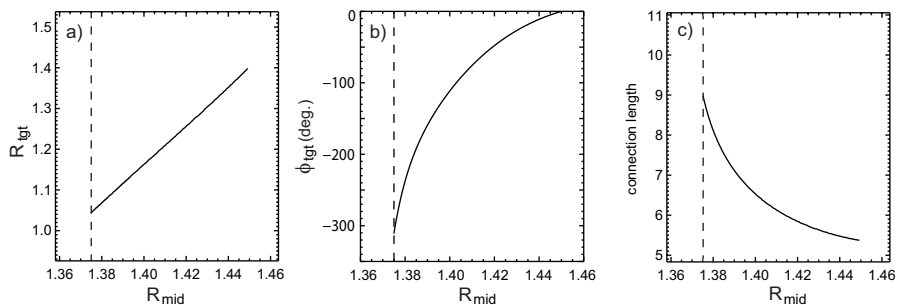


Figure 11. Mapping of the midplane radius to a) the radius at the target, b) the distance travelled toroidally between the midplane and the divertor and c) the connection length as a function of midplane location. The curves are generated by field line tracing through the equilibrium magnetic field.

4.2. Derivation of the midplane toroidal filament extent

In order to efficiently map between the target and the midplane, a parameterisation of the equilibrium magnetic field can be made so that the midplane position from a given divertor position can be determined without the need for field line tracing. The

parameterisation used for the data in this paper is shown in figure 11 and is generated by field line tracing radially across the midplane [16]. The parameterisation shows the field lines are strongly sheared by the X point, which acts to elongate the filaments as they travel from the midplane to the divertor.

The shearing of the filaments due to the equilibrium magnetic field is illustrated in figure 12 where a set of points are mapped from the midplane to the divertor and the intersection of the points with horizontal and (R,Z) planes are plotted. The filament at the midplane is circular in cross section and is distorted by the field as it travels to the divertor, the points nearer to the LCFS are displaced a greater distance in toroidal angle than those on the outboard side of the filament, giving the shear of the filament seen in the figure 12 a). The tracing shows that the shear changes the cross section from circular at the midplane (black circle) to elongated into an arc at the divertor (gold diamonds) as can be seen in figure 12 a). Figure 12 panel b) shows the filament shape at it intersects the (R,Z) plane at a range of toroidal angles during its path to the divertor. The shearing of the filament can be seen clearly in this figure, with the filaments narrowing perpendicular to the magnetic field and extending toroidally, and is responsible for generating the filament pattern seen at the divertor in the IR. The data shown in figure 12 panel b) shows a single filament at multiple toroidal angles around the machine, which is equivalent to following multiple filaments and plotting where they intersect a single plane in toroidal angle. As the figure shows, the filaments at the divertor are narrow in radial extent and occur in bands across the divertor at various radii, this has been previously seen in visible imaging [16] and are seen in the IR data presented here.

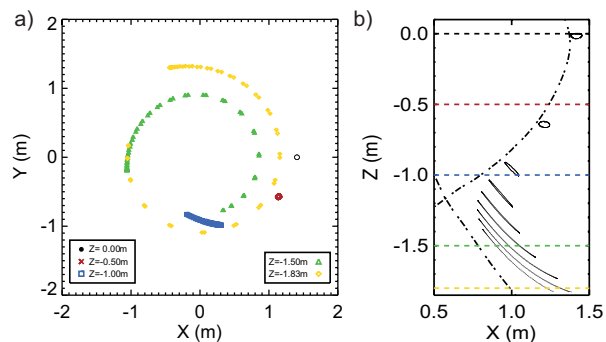


Figure 12. The intersection of the field line from a set of points at the outboard midplane with the horizontal and poloidal planes. Panel a) shows the intersection of 50 points from the midplane with different horizontal planes in the plasma. The location of the horizontal planes are shown by the dashed lines on panel b). Panel b) shows the intersection of 350 midplane points with the (R,Z) plane at a range of toroidal angles.

Previous studies have determined the filament diameter perpendicular to the equilibrium magnetic field lines at the outboard plasma midplane. The perpendicular filament toroidal extent (L_{\perp}^{mid}) is given by equation 3 where α is the field line pitch at the midplane outboard side ($\alpha \approx 20^\circ$ for this equilibrium). The perpendicular

filament toroidal extent can be derived from the divertor radial width of the the filaments measured by the IR.

$$L_{\perp}^{mid} = R_{mid}\delta\phi_{mid}\sin\alpha \quad (3)$$

If the conservation of flux between the midplane and the divertor is considered, then the area at the target, A_{tgt} , is related to the area at the midplane, A_{mid} as $A_{tgt} = A_{mid}A_{exp}$ where B_{exp} is a factor that accounts for the flux expansion and the change in radius from the target to the divertor. The midplane toroidal size of the filament in the horizontal plane is given by the angular size of the filament, $\delta\phi_{mid}$, and the radius at which the filament is located, R_{mid} . Thus, the area of the filament is the toroidal size multiplied by the radial size, δR_{mid} , such that $A_{mid} = (R_{mid}\delta\phi_{mid})\delta R_{mid}$ for the midplane and similarly for the divertor. Therefore, the conservation of filament area between midplane and target and conversion between horizontal filament size and perpendicular width (equation 3) gives the relation shown in equation 4.

$$(R_{tgt}\delta\phi_{tgt})\delta R_{tgt} = \frac{L_{\perp}^{mid}}{\sin\alpha}\delta R_{mid}B_{exp} \quad (4)$$

The area expansion, B_{exp} , can be determined by considering that the area of an annulus at the midplane and the divertor differ by the multiple of B_{exp} , giving an expression for B_{exp} shown in equation 5.

$$B_{exp} = \frac{R_{tgt}dR_{tgt}}{R_{mid}dR_{mid}} \quad (5)$$

The conservation of flux can be used to determine an expression for dR_{tgt}/dR_{mid} in terms of quantities accessible from the equilibrium field. Equation 6 shows the conservation of the flux through an annulus at the midplane and target, which can be rearranged to give an expression for dR_{tgt}/dR_{mid} (equation 7). Equation 7 is equivalent to the flux expansion, f_{exp} , between the midplane and the target [25]. Therefore the final expression for the area expansion is that given by equation 8.

$$2\pi R_{mid}dR_{mid}B_{mid}^{\perp} = 2\pi R_{tgt}dR_{tgt}B_{tgt}^{\perp} \quad (6)$$

$$\frac{dR_{tgt}}{dR_{mid}} = \frac{R_{mid}B_{mid}^{\perp}}{R_{tgt}B_{tgt}^{\perp}} = f_{exp} \quad (7)$$

$$B_{exp} = \frac{R_{tgt}f_{exp}}{R_{mid}} \quad (8)$$

Combining equations 4 and 8 and rearranging, an expression for the midplane perpendicular size can be derived (equation 9) from quantities which are measured experimentally or derived from the equilibrium field. In equation 9 the quantity $\frac{d\phi_{tgt}}{dR_{mid}}$ is determined using the result of the field line tracing shown in figure 11 and is evaluated at the target location of the filament being analysed. The variation of this quantity across the divertor is shown in figure 13 as a function of distance from the LCFS and for two different times during the discharge. The profile is obtained by differentiation

of the curves shown in figure 11. In order to gather a sufficient number of filaments to make the results statistically significant, filaments have been extracted from a 100 ms period of the discharge. The solenoid fringing field on MAST is not completely cancelled by the poloidal field coils and as such there is an associated sweeping of the strike point and modification of the equilibrium during this period. The strike point sweeping can be clearly seen in figure 2 as the increase in radius of the peak of the heat flux in time. Obviously, variation in the equilibrium can affect the parameterisation of the field. The two curves in figure 13 represent the parameterisation at the start and end of the region where the data is extracted. Using the parameterisation in terms of ΔR_{LCFS} removes the effect of the strike point sweeping and variation of the field. Therefore, a parameterisation from a single time is used to convert all of the data to improve the speed of analysis and prevent the requirement for field line tracing through the equilibrium for each time point analysed. The numerical field line tracing can also introduce an error, especially for structures as small as the filaments seen at the divertor (of the order 5 mm). It is possible to obtain an estimate of the error on the derived size using the difference between the two mappings in figure 13 at a given δR_{LCFS} and in the numerical field line following by varying the step size in the mapping. The resulting error from these two sources amounts to 5% to 15% from $\Delta R_{LCFS} = 0.05$ m to $\Delta R_{LCFS} = 0.15$ m which is the range over which the filaments are extracted.

$$L_{\perp}^{mid} = \frac{R_{mid}}{f_{exp}} \left(\frac{d\phi_{tgt}}{dR_{mid}} \right) \sin \alpha \delta R_{tgt} \quad (9)$$

The flux expansion, f_{exp} , can be determined using field line tracing by taking the derivative of the data shown in figure 11 a). The flux expansion given as $\frac{dR_{mid}}{dR_{tgt}}$ which varies with distance from the LCFS. The value of f_{exp} used in the conversion from target width to midplane width is performed using the flux expansion determined using this derivative at the location of the filament in terms of ΔR_{LCFS} .

5. Analysis of the filament data at the midplane

The techniques described in section 4 can be used to determine the filament properties at the midplane using the IR measurements at the target which were presented in section 3. In this section the toroidal mode number of the filaments will be determined using the IR data, the toroidal extent at the midplane will be determined and the radial midplane extent inferred.

Analysis of the data in this section requires filtering of the data due to limitations in the measurements. The large amount of shear near the X point gives rise to closely spaced filaments which the IR spatial resolution prevents being fully resolved and produces abnormally large midplane toroidal extents when converted using the method described in the preceding section. Whilst filaments in the outer SOL have sufficient spatial separation to be resolved by the camera, the heat flux in these filaments introduces an additional restriction in the far SOL as there is insufficient

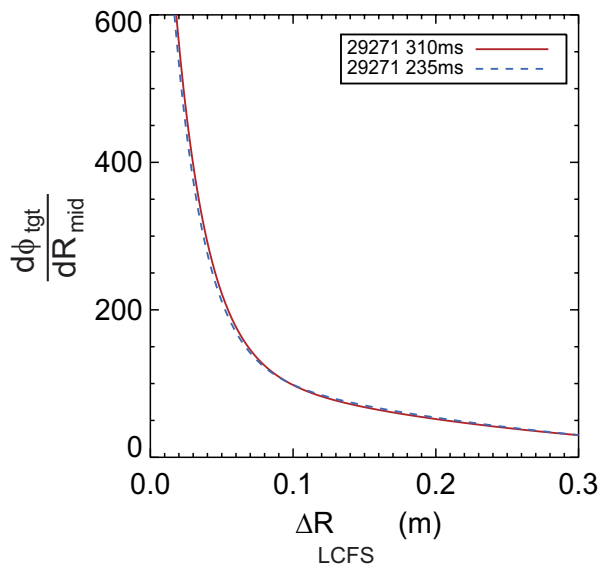


Figure 13. Comparison of the quantity $\frac{d\phi_{tgt}}{dR_{mid}}$ which is used to map the radial target filament width into the toroidal midplane filament angular size. The plot compares the mapping at two different times in the discharge with the target radius converted into the distance from the last closed flux surface, ΔR_{LCFS} .

signal to locate and fit the filament width. These considerations have led to the region $0.05 \text{ m} \leq \Delta R_{LCFS} \leq 0.15 \text{ m}$ being defined as the region in which the filaments are sufficiently resolved to determine the midplane extent.

5.1. Filament size

The filament radial size at the target, δR_{tgt} , shown in figure 8 can be converted into a perpendicular extent at the midplane, using equation 9. Figure 14 shows the perpendicular toroidal filament diameter at the midplane determined from the IR data. The modal value for the filament size is 3-5 cm, which is smaller than the 7-9 cm determined from previously published visible imaging measurements [14], although the IR data shows a broad range of values returned, with a standard deviation of 5 in the filament size. The radial size cannot be directly measured using the IR data, as this would require the determination of the toroidal extent of the filament at the divertor which is not possible with the field of view of the IR data, assuming that the start and end of a given filament could be identified. However, it should be noted that the visible imaging suggests that the midplane filaments are approximately circular in cross section. Therefore, by using the visible midplane measurements to interpret the results from the IR data, the radial filament size at the midplane (L_{rad}^{mid}) can be taken to be equal to the toroidal size, L_{\perp}^{mid} .

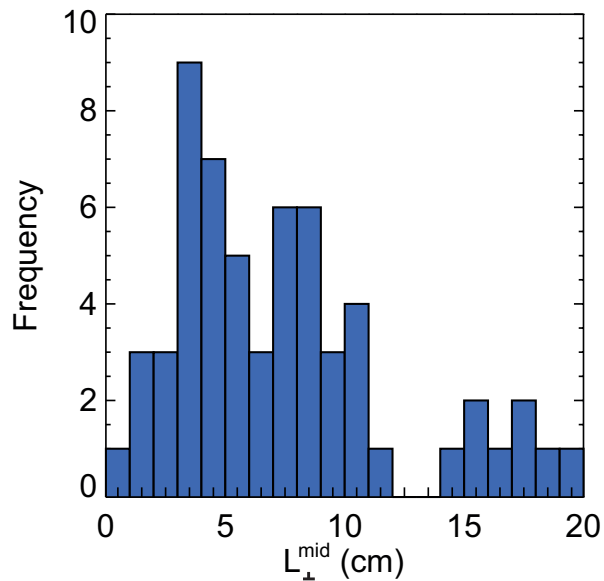


Figure 14. Histogram showing the distribution of filament sizes measured at the midplane LCFS, perpendicular to the equilibrium magnetic field (L_{\perp}^{mid}).

5.2. Quasi toroidal mode number

Past measurements of the filaments in L mode plasmas on MAST [14] has shown that they exhibit a global structure, whereby a number of filaments can be seen to exist over one camera integration period. Naturally, the turbulence that generates the filaments will have a spectrum of mode numbers, but following the previous analysis of visible filaments [14] and IR analysis of ELM filaments [23] a quasi mode number, n , can be determined which is simply the number of filaments observed at any one time.

The filament quasi toroidal mode number has been determined previously from IR measurements of ELMs in both ASDEX Upgrade [23] and JET [24] with the assumption that the filaments are evenly spaced at the midplane and emerge simultaneously from the midplane. The determination of the filament quasi toroidal mode number, n , is performed using field line tracing from the radial position of the peak of each identified filament to the specific toroidal angle at the midplane. Using this mapping on a number of consecutive profiles exhibiting filaments, a plot as shown in figure 15 can be generated showing the toroidal angle for each filament versus the filament index. Figure 15 shows the filament toroidal angles extracted from fifteen IR profiles, where the abscissa is the index of the filament (increasing index with radius and frame) identified and provides direct evidence for the mode number of the filaments from the IR measurements. The groups of points in figure 15 correspond to the filaments in an individual IR profile and can be seen to be clustered into groups with similar spacing in toroidal angle which shows that a set of consecutive filaments has been identified. Filaments located with large or irregular spacing near to the LCFS and far into the SOL have been removed as these likely result from missing filaments which are too low in heat flux or narrow in width to be identified at the far ends of the IR profile. The mode number of the

filaments can be estimated from the gradient of each group of points in figure 15 by fitting a straight line through a set of points (solid blue line) and then determining the intercept between the dashed lines which represent a full toroidal circumference of the machine. The mode number estimate is the difference between the abscissa index of the intercepts, which in the example shown gives $n=17$. As can be seen in the figure, there is some variation of the mode number for the filaments shown, with the shallower gradient indicating higher toroidal mode numbers.

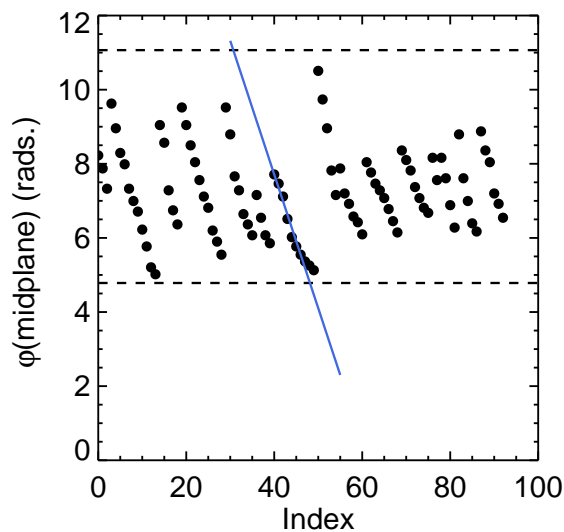


Figure 15. The midplane toroidal angle at which filament peaks have been located, as a function peak number. The bands of points correspond to the fifteen profiles where filaments have been extracted. The dashed lines represent a spacing in toroidal angle of 2π radians. The solid blue line is a fit to a set of points from one profile, the intersection between this line and the dashed line provides an estimate of the toroidal mode number.

The mode number can also be determined using equation 10 [23], where the separation in angle between adjacent filaments, $\Delta\phi$, is averaged over the number filaments in a given profile where a is the number of filaments. This technique is more suited to automated analysis of the filament mode number and has been applied to the filaments shown in figure 15.

$$n = \frac{1}{a} \sum_{i=1}^a \frac{2\pi}{\phi_i - \phi_{i+1}} = \frac{1}{a} \sum_{i=1}^a \frac{2\pi}{\Delta\phi} \quad (10)$$

The mode number determined in this manner spans the range $7 < n < 22$ with an average mode number of $n=13$. The estimate of the mode number at the midplane from visible imaging is $20 < n < 50$, which is larger than the average mode number determined from the IR data. However, there is some overlap in the range of values seen from the IR measurements and the visible measurements. The discrepancy between the visible and the IR values could arise for a number of reasons. Firstly, the visible

data observes the filaments at the midplane, whilst they are attached to the plasma and rotating around with the plasma. The filament pattern at the divertor is composed of filaments that have detached from the plasma edge and are depositing power onto the divertor surface. The detached phase is marked by the filaments moving radially outwards from the plasma edge; it is this radial motion that generates the spiral structures imaged with the IR camera [16]. The filaments may not all detach from the plasma and propagate outwards at the same time, which will change the mode number seen at the divertor. The observation of a decreasing in the toroidal mode number with increasing distance from the last closed flux surface is supported with modelling which has also identified this trend [26]. Secondly, the maximum mode number which can be observed relies upon the spatial resolution of the IR measurements at the target, which is limited by both the camera but also the ability to resolve two separate filament peaks.

$$n_{max} = 2\pi \left(\frac{d\phi_{mid}}{dR_{tgt}} \right)^{-1} \Delta R_{min} \quad (11)$$

The maximum observable mode number which can be determined by considering the required filament separation and the rate of change of the midplane toroidal angle with target location. Equation 11 is used to determine the maximum mode number, where $\frac{d\phi_{mid}}{dR_{tgt}}$ relates the midplane angle with the target location and is obtained from field line tracing. The fitting of the filaments with a Gaussian profile to determine the width requires at least 5 points to ensure a good fit with a Gaussian of 4 terms. Therefore, this sets the minimum separation between two adjacent filament peaks, ΔR_{min} , to be four times the IR spatial resolution, equivalent to 6.4 mm. The maximum observable mode number varies over the target radius where the filaments are located. The typical maximum mode number is 40 at $\Delta R_{LCFS} = 0.1\text{m}$, but can be as low as 18 at $\Delta R_{LCFS} = 0.05\text{m}$. Therefore, the discrepancy between the IR and visible mode numbers could be due to the limitation of the maximum mode number observable using the IR data.

5.3. Direct comparison of the filament properties between the IR and visible imaging

It is instructive to make a direct comparison of the visible filament width using data from the same discharge where the IR data has been analysed. High speed midplane imaging data has been taken in this discharge with a frame rate of 1 kHz and an integration time of 1 μs , which allows filament width to be determined from visible imaging. The analysis method used for the data follows that described by Ayed et al [14] and allows the toroidal perpendicular filament width and mode number to be extracted. The toroidal mode number derived from the visible analysis is $n=20$, which is consistent with the previous studies across several discharges and lies within the range of mode number identified by the IR analysis. The mean IR mode number ($n=13$) is lower than the visible, however, as detailed above, the visible imaging determines the mode number in the attached phase where the mode number is expected to be higher than the detached phase observed by the IR.

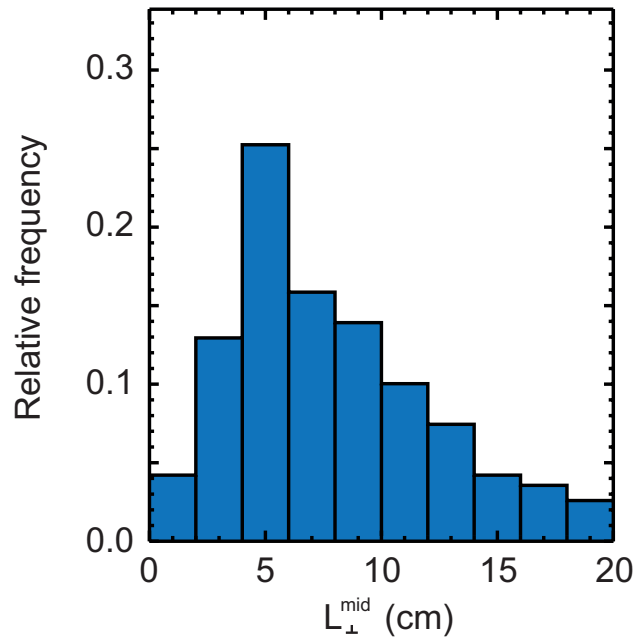


Figure 16. Histogram of the perpendicular filament size derived from visible imaging at the midplane.

Figure 16 shows a histogram of the filament perpendicular size at the midplane from visible imaging analysis, which can be directly compared to the equivalent IR data shown in figure 14. The visible imaging gives a modal filament size to be 4-6 cm, which is in agreement with the widths derived from the IR data. The range of variation seen in the visible data is smaller than that observed in the IR data, this is likely due to the shorter integration time of the visible camera to the IR camera would also lessen any effect toroidal rotation will have on the derived width. In addition to the effect of integration time, the IR width relies on additional information, such as the magnetic field geometry and heat flux to the target to determine the width. These additional parameters can introduce variation in the derived width, increasing the range of values observed. By contrast, the visible filament width is directly measured at the midplane, which decreases the number of sources of error in the value obtained. The agreement in filament width between the visible data and the IR data shows that the method of extracting the midplane measurements from the heat flux at the divertor is robust.

5.4. Effect of toroidal plasma rotation

Toroidal rotation of the filaments in the field of view of the IR camera will affect the width of the filaments measured, unless the duration of the filament is shorter than the integration time of the IR camera. The L mode filaments have been observed to rotate at typical velocities of 2-9 km/s at the outboard midplane of MAST [14], which during the integration time of the camera is a toroidal distance of 6 to 27 cm. The toroidal velocity at the LCFS, as measured by charge exchange recombination spectroscopy (CXRS) [27], varies between 3-8 km/s in this discharge, although the value is sensitive to the exact

location of the LCFS.

The toroidal rotation at the midplane will give a radial motion of the filaments at the divertor and generates broadening in the IR profiles. In order to understand the effect the toroidal rotation velocity has on the on the IR filament measurements, a model has been developed of the filament rotation. The model takes a regular grid of points at the divertor in (r, ϕ) coordinates and maps these points to the midplane to determine the heat flux expected at the target. The heat flux at a given position in this target grid can then be determined using a periodic heat flux at the midplane as defined by equation 12, consisting of filaments with a certain size radially, σ_r , toroidally, σ_ϕ and mode number, n . The assumption of this model is that the filaments are Gaussian in profile, born at a set radius (r_0) which is separated from the LCFS and that there is no loss of heat flux between midplane and target. Furthermore, it is assumed that the filaments propagate toroidally at a fixed speed, which is consistent with visible imaging measurements of the filament motion [4].

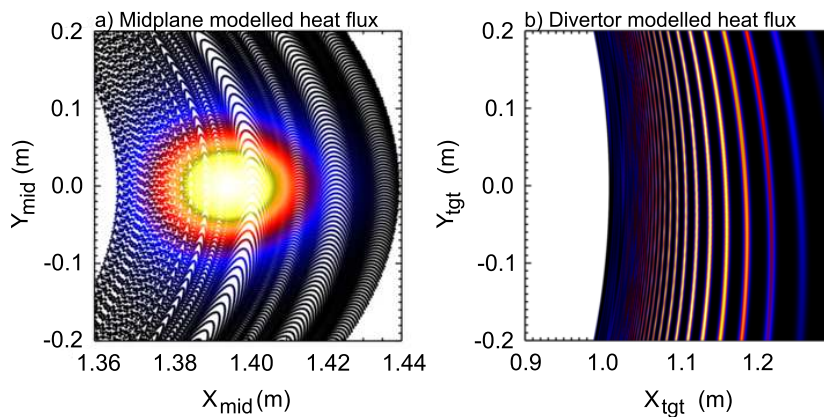


Figure 17. Output from a filament model to investigate the effect of toroidal rotation. Panel a) shows the modelled midplane filament size in the horizontal plane and panel b) shows the resulting footprint at the divertor from 15 filaments. The modelling grid is regularly spaced at the divertor and as a result irregularly gridded at the midplane. The irregular midplane grid is the cause of the bands in a).

The data shown in figure 17 shows the filament horizontal cross section at the midplane in panel a) which is used as input to the model. The filament is plotted in the horizontal cross section, which acts to elongate it in the toroidal direction (vertically in the figure). The model uses $n=15$, matching the range of mode numbers seen experimentally from the IR data, to generate a footprint at the target from the filament which is shown in panel b). The modelled filament footprint is consistent with the data seen experimentally, showing the banding originating from the midplane filaments. The filament is no longer connected to the plasma in the model, which is known as the detached phase. The model in the detached phase only accounts from the power carried

by the filament and not diffusing from the plasma.

$$q_{mid}(r, \phi) = \exp\left(-\frac{\pi \sin\left(\frac{n}{2}\phi\right)}{\frac{n}{2}\sigma_{phi}^2}\right) \exp\left(-\frac{\pi (r - r_0)^2}{\sigma_r^2}\right) \quad (12)$$

The modelled target profile can be extracted from figure 17 by extracting the profile across the horizontal. The resulting profiles are shown in figure 18 for a filaments with a range of toroidal velocities in the range observed for the L mode filaments. The filament extent in the toroidal and radial directions at the midplane have been defined by the experimental measurements to give a circular filament of 7 cm cross sectional diameter at the midplane, parallel to the magnetic field lines. The filament is displaced from the LCFS by 2 cm. The effect of the rotation on the IR profiles can be seen by the increase in the minima between the filaments, a decrease in the filament peak heat flux and an increase in the filament width as the toroidal rotation is increased. Figure 18 also shows that the filaments close to the LCFS begin to merge together at positions close to the divertor LCFS location ($\delta R_{LCFS} \leq 0.05$)m, this is consistent with the IR profiles which indicate that individual filaments are difficult to discriminate at low values of ΔR_{LCFS} .

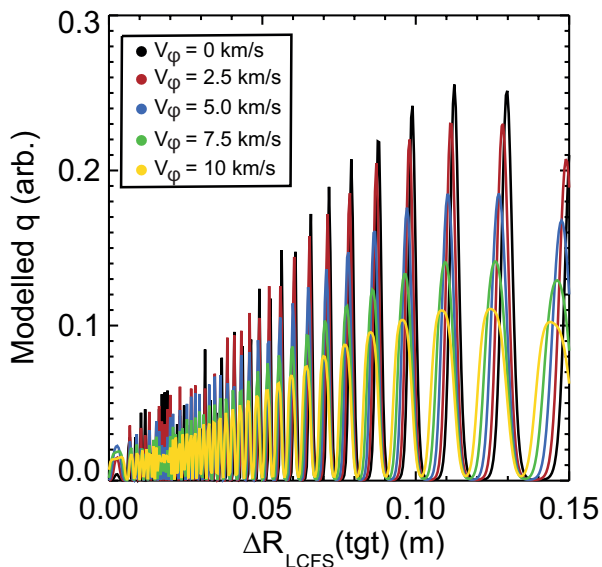


Figure 18. Modelled filament profiles at the divertor for a range of toroidal filament velocities and an integration time of $30\mu\text{s}$.

The filament width at the divertor, δR_{tgt} , can be extracted from the modelled profiles and this quantity is shown in figure 19, as a function of distance from the LCFS at the target. The filament size can be seen to decrease as the separatrix is approached due to the shear generated by the X point, the widths are also smaller in the model than those seen experimentally. One reason for the modelled sizes not matching the measured sizes is that the model does not include any diffusion which would act to broaden the filament width at the divertor. The effect of diffusion on the profiles would

be equal for all of the toroidal rotation speeds, therefore, the relative error between the stationary filament and the rotating filament can be determined using the modelled data. The fractional error for a given rotation speed and a $30 \mu\text{s}$ integration time is shown in figure 20 and can exceed 100% at the largest observed rotation velocities. The error in the measured filament size has been calculated at a range of different values of ΔR_{LCFS} , as the filament size is seen to vary as a function of the distance into the SOL. The data in figure 20 shows that the fractional error is not a function of ΔR_{LCFS} , as both the width of the filament and the error induced by the rotation scale linearly with the toroidal rotation velocity. Hence, the fractional error in the filament width as a function of the toroidal rotation velocity can be fitted with a single curve for all distances into the SOL.

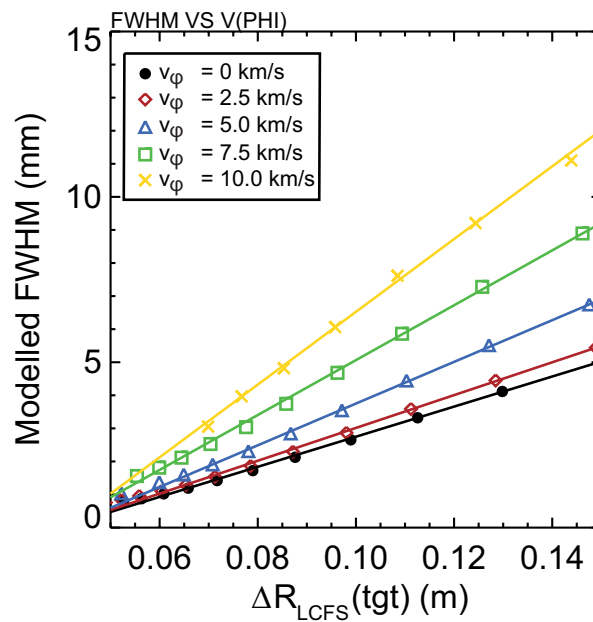


Figure 19. The filament radial width across the divertor, determined from modelled profiles with a range of toroidal rotation velocities.

The model shows that the error in the filament width could be significant, based on the assumption that the filament duration is of the order the integration time of the camera and the filaments rotate at a velocity of the plasma edge. Previous analysis of L mode filaments at the plasma edge has shown that they rotate at the plasma edge velocity and remain constant in velocity as they travel outwards into the SOL [14]. The observations of ELM filaments have shown that they are largely unaffected by the integration time of the IR camera, which would suggest that the duration of the ELM filaments is shorter than the integration time of the camera [23]. The ELM filament widths were analysed as a function of the camera integration time to assess the impact of toroidal rotation. In the L mode data presented in this analysis, the range of integration times is too small to allow a similar analysis technique. However, an alternative method can be used with the data available, using the fact that the toroidal rotation velocity of

the plasma varies in time during the analysis period.

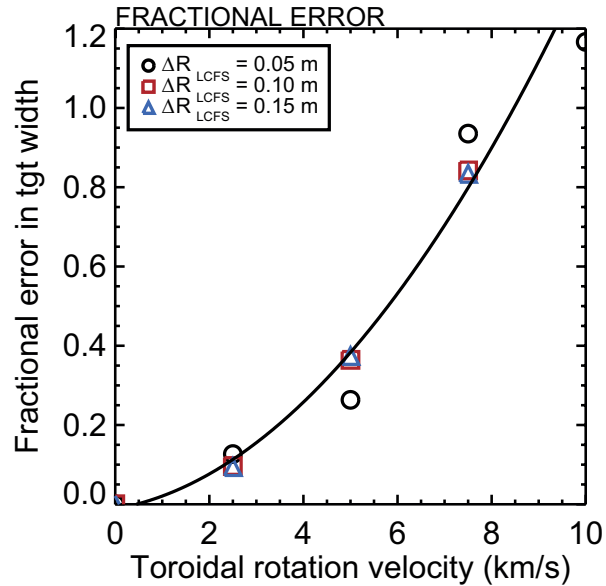


Figure 20. Fractional error on the toroidal perpendicular extent as a result of changing toroidal rotation. The plot assumes that the integration time is 30 μ s and the filament moves throughout this period.

Figure 21 shows the derived filament width for all of the filaments analysed in the discharge as a function of the toroidal rotation velocity, v_ϕ , at the LCFS. The rotation velocity has been determined using the edge position derived from a linear D α array and measurements of the rotation profiles from CXRS. The range of variation in the rotation velocity is in the range 0.5 to 8 km/s. The error expected on the measurement, as shown in figure 20, is a strong function of the toroidal velocity across the range seen in the discharge. As can be seen in figure 21, the strong trend of increasing width with increasing rotation velocity predicted by the modelling is not reproduced. This observation would suggest that the rotation velocity does not have a significant impact on the derived filament widths. However, the increased spread of the points in figure 21 suggests that there is a small, but measurable, effect of rotation on the derived widths. One interpretation of the observation that there is little effect of toroidal rotation on the derived width is that the L mode filament duration is shorter than the camera integration time, in agreement with the observations of ELM filaments. Visible imaging has also shown that the L mode filament duration is shorter than the ELM filament duration [15], as the ELMs are unaffected by the toroidal rotation (as shown by Eich et al [23]), then it would follow from the relative durations between these events that the L mode filaments should also be unaffected by the rotation.

widths using visible imaging, as these measurements were performed at the midplane. However, it has been shown that the midplane width can be derived from the IR target width measurement using a parameterisation of the equilibrium magnetic field. This then allows the determination of the midplane filament size from the IR data. The application of the parameterisation to the measured width has determined the midplane width of the filaments to be 3-5 cm (± 5 cm) which is similar to the 7-9 cm derived from previously published measurements from visible imaging. Measurements of the visible filament width in the same discharge the IR is analysed in show a perpendicular size of the order 4-6 cm, in good agreement with the IR data. The separation between the filaments at the target can be used to determine the quasi mode number which is a measure of the number of the filaments in a given profile (assuming evenly distributed filaments). The average observed mode number is $n=13$, with a range of $7 < n < 22$ which is smaller than the visible measurements. The variation of the mode number over such a large range could be explained by the mechanism by which the filaments are emitted. The filaments are ejected independently in time, the imaging data records a given number of filaments at any one instance and the mode number (number of filaments seen) varies from profile to profile. The discrepancy between the observed mode number may also arise due to the visible filaments being observed at the stage where they are attached to the plasma edge and the IR measurements performed on those filaments which have detached. The detachment of the filaments from the plasma edge and the propagation outwards into the SOL may not occur at the same time for all filaments, and this would give rise to a lower toroidal mode number. In addition, the IR camera system is limited in the maximum mode number that can be observed by the spatial resolution of 1.6 mm/pixel and the requirement of enough points in a filament peak to generate an acceptable Gaussian fit. The widths and mode number derived from the IR data agree both with the previous visible imaging measurements performed over a range of discharge, but also with visible analysis of high speed imaging in the same discharge the IR data is taken in. The agreement between the visible data and IR data from the same discharge shows that the method of extracting the widths from the filament size at the divertor is robust.

Finally, the effect of toroidal rotation on the measured filament at the divertor has been investigated by using a simple filament model. The effect of toroidal rotation has seen to be significant in the modelling, with broadening of the filament width in excess of 100% seen for the highest rotation velocities, assuming the filament duration is of the order the camera integration time. However, comparison of the measured widths as a function of toroidal rotation velocity does not match that observed with the modelling. The measurements suggest that toroidal rotation does not affect the measured width significantly which could indicate that the filament duration is shorter than the camera integration time, as is the case with ELM filament observations.

The measured filament widths, combined with the measured heat flux fall off length $\lambda_q = 6.3$ mm show that the filaments are much larger at the midplane than the fall off length. The typical filament heat flux is between 0.6 and 0.8 MW/m² and the integral

of the filament heat flux in the region where the filaments can be individually identified amounts to 0.14 (± 0.1) MW. These observations suggest that the power carried to the outer divertor (beyond the region dominated by the fall off length) is small, but is dominated by the filaments. The observation that the total power from filaments is small is beneficial for the first wall power handling in present and future devices.

Acknowledgments

This work has been carried out within the framework of the EUROfusion Consortium and has received funding from the Euratom research and training programme 2014-2018 under grant agreement No 633053 and from the RCUK Energy Programme [grant number EP/I501045]. To obtain further information on the data and models underlying this paper please contact PublicationsManager@ccfe.ac.uk. The views and opinions expressed herein do not necessarily reflect those of the European Commission.

References

- [1] SJ Zweben et al. Edge turbulence measurements in toroidal fusion devices. *Plas. Phys. Control. Fusion*, 49:S1–S23, 2007.
- [2] JL Terry et al. Transport phenomena in the edge of Alcator C-Mod plasmas. *Nucl. Fusion*, 45:1321–27, 2005.
- [3] SJ Zweben et al. Structure and motion of edge turbulence in the National Spherical Torus Experiment and Alcator C-Mod. *Phys. Plasmas*, 13:056114, 2006.
- [4] A Kirk et al. Filamentary structures at the plasma edge on MAST. *Plas. Phys. Control. Fusion*, 48:B433–B441, 2006.
- [5] C Silva et al. Intermittent transport in the JEL far SOL. *J. Nucl. Mater.*, 390-391:355–8, 2009.
- [6] JA Boedo et al. Transport by intermittency in the boundary of the DIII-D tokamak. *Phys. Plasmas*, 10:1670, 2003.
- [7] HW Muller et al. Latest investigations on fluctuations, ELM filaments and turbulent transport in the SOL of ASDEX Upgrade. *Nucl. Fusion*, 51:073023, 2011.
- [8] D Carralero et al. An experimental investigation of the high density transition of the scrape off layer transport in ASDEX Upgrade. *Nucl. Fusion*, 54:123005, 2014.
- [9] N Fedorczak et al. Electrostatic transport in L-mode scrape-off layer plasmas of Tore Supra tokamak. II. Transport by fluctuations. *Phys. Plasmas*, 19:072314, 2012.
- [10] F Militello et al. Experimental and numerical characterization of the turbulence in the scrape-off layer of MAST. *Plasma Phys. Control. Fusion*, 55:025005, 2013.
- [11] OE Garcia et al. Computations of intermittent transport in scrape-off layer plasmas. *Phys. Rev. Lett.*, 92:165003, 2004.
- [12] DA D’Ippolito et al. Cross-field blob transport in tokamak scrape-off layer plasmas. *Phys. Plasmas*, 9:222, 2002.
- [13] I Katramados et al. MAST-Upgrade closed pumped divertor design and analysis. *Fusion Eng. Des.*, 86:1595–1598, 2011.
- [14] N Ben Ayed et al. Inter-ELM filaments and turbulent transport in the Mega Amp Spherical Tokamak. *Plas. Phys. Control. Fusion*, 51:035016, 2009.
- [15] BD Dudson et al. Experiments and simulation of edge turbulence and filaments in MAST. *Plasma Phys. Control. Fusion*, 50:124012, 2008.
- [16] A Kirk et al. Evolution of the pedestal on MAST and the implications for ELM power loadings. *Plas. Phys. Control. Fusion*, 49:1259–75, 2007.

- [17] JR Harrison et al. L-mode and inter-ELM divertor particle and heat flux width scaling on MAST. *J. Nucl. Mater.*, 438:S375–8, 2013.
- [18] G De Temmermann et al. Thermographic studies of heat load asymmetries during MAST L-mode discharges. *Plasma Phys. Control. Fusion*, 52:095005, 2010.
- [19] A Herrmann et al. Limitations for divertor heat flux calculations of fast events in tokamaks 27th conf. to plasma physics and controlled fusion (Madeira, Portugal). In *Proc. EPS 2001*, 2001.
- [20] E Delchambre et al. Effect of micrometric hot spots on surface temperature measurement and flux calculation in the middle and long infrared. *Plasma Phys. Control. Fusion*, 51:055012, 2009.
- [21] T Eich et al. Inter-ELM power decay length for JET and ASDEX Upgrade: measurement and comparison with heuristic drift-based model. *Phys. Rev. Lett.*, 107:215001, 2011.
- [22] LL Lao et al. Reconstruction of current profile parameters and plasma shapes in tokamaks. *Plasma Phys. Control. Fusion*, 25:1611, 1985.
- [23] T Eich et al. Type-I ELM substructure on the divertor target plates in ASDEX Upgrade. *Plasma Phys. Control. Fusion*, 47:815, 2005.
- [24] S Devaux et al. Type-I ELM filamentary heat load patterns on the divertor target at JET. In *36th EPS Conference on Plasma Phys. Sofia ECA Vol.33E, P-2.157*, 2009.
- [25] A Loarte et al. Multi-machine scaling of the divertor peak heat flux and width for L-mode and H-mode discharges. *J. Nucl. Mater.*, 266-269:587–592, 1999.
- [26] B Dudson. *Edge turbulence in the Mega Amp Spherical Tokamak*. PhD thesis, University of Oxford, 2007.
- [27] NJ Conway et al. High-throughput charge exchange recombination spectroscopy system on MAST. *Rev. Sci. Inst.*, 77:10F131, 2006.